

SAT-HMR: Real-Time Multi-Person 3D Mesh Estimation via Scale-Adaptive Tokens

Chi Su¹ Xiaoxuan Ma¹ Jiajun Su² Yizhou Wang¹

¹Peking University ²International Digital Economy Academy (IDEA)

suchi@stu.pku.edu.cn, {maxiaoxuan, yizhou.wang}@pku.edu.cn, sujiajun@idea.edu.cn

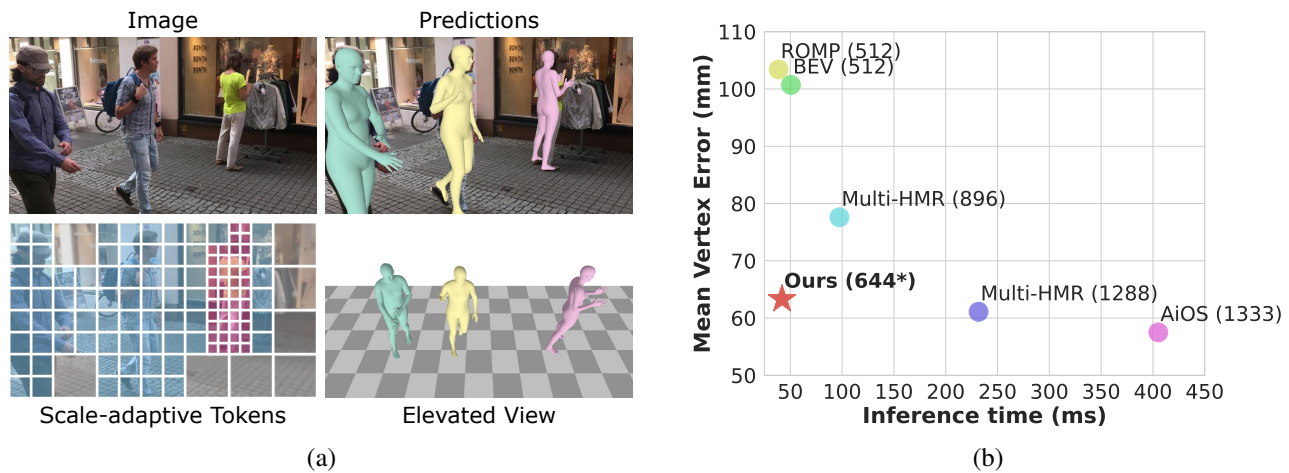


Figure 1. (a) We propose scale-adaptive tokens in our one-stage framework for real-time multi-person 3D mesh estimation. Our method introduces scale-adaptive tokens, dynamically adjusted based on the relative size of individuals in the image, to more efficiently encode features, enabling real-time and accurate multi-person mesh estimation. We present a conceptual visualization of the scale-adaptive tokens. The right column visualizes the predicted meshes projected onto an image from 3DPW [48] dataset and from an elevated view. (b) Comparison of estimation error and inference time across different methods, with input resolutions in parentheses. Our method, using a mixed resolution with a base resolution of 644, achieves comparable performance to state-of-the-art methods on AGORA [32] test set while maintaining real-time inference efficiency.

Abstract

We propose a one-stage framework for real-time multi-person 3D human mesh estimation from a single RGB image. While current one-stage methods, which follow a DETR-style pipeline, achieve state-of-the-art (SOTA) performance with high-resolution inputs, we observe that this particularly benefits the estimation of individuals in smaller scales of the image (e.g., those far from the camera), but at the cost of significantly increased computation overhead. To address this, we introduce scale-adaptive tokens that are dynamically adjusted based on the relative scale of each individual in the image within the DETR framework. Specifically, individuals in smaller scales are processed at higher resolutions, larger ones at lower resolutions, and background regions are further distilled. These scale-adaptive tokens more efficiently

encode the image features, facilitating subsequent decoding to regress the human mesh, while allowing the model to allocate computational resources more effectively and focus on more challenging cases. Experiments show that our method preserves the accuracy benefits of high-resolution processing while substantially reducing computational cost, achieving real-time inference with performance comparable to SOTA methods. Code and models are available at <https://ChiSu001.github.io/SAT-HMR/>.

1. Introduction

Multi-person 3D human mesh estimation from a single RGB image aims to localize all individuals in the scene and estimate their 3D meshes, typically represented by a parametric human model such as SMPL [24]. This is a fundamental task

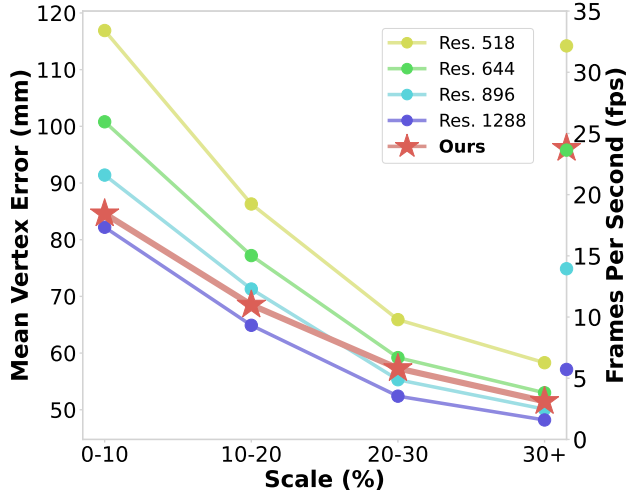


Figure 2. **Estimation errors and FPS of baselines with different resolutions and our method across individuals at various scales.** The scale of an individual refers to the person’s size relative to the overall image and please refer to Sec. 3.3 for mathematical definition. The colored lines show the Mean Vertex Error (MVE) errors (left y-axis) of the baselines with different resolutions (Res.) on the AGORA [32] validation set. The colored markers on the right y-axis indicate the FPS of the corresponding models. Our method adopts a mixed resolution with a base resolution of 644.

with broad applications, spanning social interaction [41, 58], game production [59], *etc.* Existing methods primarily focus on addressing challenges such as monocular depth ambiguity and inter-person interactions, and can be broadly categorized into two types: multi-stage and one-stage approaches. Multi-stage methods [7, 14, 34, 53, 54] typically detect and process each individual by cropping and resizing them to a uniform, relatively high resolution, which generally improves performance. However, this overlooks the global context, such as the original scales of individuals and their relative positions within the entire image, potentially leading to suboptimal results.

To address these limitations, one-stage methods gradually emerge as a promising alternative [2, 43–45]. These approaches operate on the entire image without explicit cropping, preserving global context and enabling end-to-end training. Building on the success of DETR [5] in object detection, recent works [2, 43] adopt a DETR-style pipeline. They mainly focus on designing queries and decoders to estimate the human mesh, *e.g.* Multi-HMR [2] uses queries to represent each person and decodes the corresponding human mesh. However, these methods rely on high-resolution inputs to achieve state-of-the-art (SOTA) results, as shown in Fig. 1 (b), which significantly increases computational cost and limits real-time processing capabilities.

Building on the findings of [2, 43], we observe that high-resolution input plays a crucial role in improving accuracy. To explore this, we design a naive baseline following similar

architecture [2] and analyze how its estimation error changes for individuals of different scales as we increase the input resolution. We define scale as the size of the person relative to the entire image¹. As shown in Fig. 2, increasing the input resolution consistently leads to a decrease in the estimation error, particularly for smaller-scale individuals (*e.g.*, those farther from the camera). Notably, for individuals in the 0-10% scale, we observe an error decrease of nearly 35mm when comparing the highest-resolution model (blueviolet) to the lowest-resolution one (yellow). However, processing the entire image at high resolution incurs significant computational costs, especially when individuals are close to the camera and occupy a large portion of the image. In such cases, these individuals are already represented by many tokens, and using more tokens with high resolution would only greatly increase the cost while offering marginal improvement (*i.e.*, a slight error reduction in cases where individuals cover 30+% of the image in Fig. 2). Therefore, both our best baseline model (blueviolet) and recent SOTA methods [2, 43] in Fig. 1 (b) fail to achieve real-time inference and run at about 5 FPS, highlighting a common limitation.

To address this, we extend our baseline built on DETR [5] and shift our focus toward more efficient feature encoding. Specifically, we introduce **scale-adaptive tokens**, which are dynamically adjusted based on the scale of individuals in the image. We first predict a patch-level scale map, assigning a scale value to each token. Tokens corresponding to smaller-scale individuals are replaced with higher-resolution tokens. Additionally, background tokens identified by the scale map are further distilled to reduce computational cost. These scale-adaptive tokens capture individuals at varying scales with the appropriate level of detail, as shown in Fig. 1 (a). The tokens are then processed by the decoder and prediction heads to regress the human mesh. By efficiently allocating computational resources to the more challenging cases, our method strikes a better balance between accuracy and speed. As shown in Fig. 2, our method (red) achieves performance comparable to high-resolution input while maintaining real-time inference speed at 24 FPS. Experiments on benchmark datasets further demonstrate the effectiveness of our method, achieving competitive performance with high efficiency.

To conclude, our contributions are as follows:

- We propose scale-adaptive tokens that are dynamically adjusted to handle individuals of varying scales, enabling more efficient feature encoding.
- By employing scale-adaptive tokens, our method achieves performance comparable to using full-image high resolution, but with significantly lower computational cost.
- Our approach achieves SOTA performance with up to 5x the speed of the top-performing methods, making it the **best real-time** model for multi-person 3D mesh estimation, running at 24 FPS.

¹See Eq. (1) for detailed definition of scale.

2. Related work

2.1. Multi-Person Human Mesh Estimation

Multi-person human mesh estimation from a single RGB image aims to regress all human meshes, typically represented by parametric models such as SMPL [24] and SMPL-X [33]. Existing methods can be categorized into *multi-stage* and *one-stage* approaches. Multi-stage methods [7, 11, 14, 34, 53, 54] use off-the-shelf human detectors [37] to crop each person’s region, followed by single-person mesh estimation [26, 49, 55, 57]. This approach preserves relatively high-resolution images for each cropped region, generally leading to higher accuracy [43]. However, its reliance on detected bounding boxes and the lack of global context make it challenging to handle occlusion [44].

In contrast, one-stage methods [2, 35, 43–45] estimate human meshes for all individuals by encoding the entire image and predicting simultaneously. Pioneer work like ROMP [44] and BEV [45] use CNN backbones [12] to extract global features for mesh regression. However, the low input resolution limits the expressiveness of the distilled features [43], leading to suboptimal performance. Recent methods like AiOS [43] and Multi-HMR [2] adopt DETR-style architectures to achieve SOTA performance at higher resolutions, but with significant computational overhead, making real-time use impractical (*e.g.*, Multi-HMR runs at only 4 FPS as shown in Fig. 1). Instead, we argue that tokenizing the entire image at high resolution is unnecessary. By adjusting patch resolution based on the scale and focusing computational resources on more challenging areas, we achieve real-time inference with competitive performance.

2.2. Transformers in Human Mesh Estimation

Transformers [47], originally designed for sequential inputs, have demonstrated strong performance in various vision tasks, such as image classification with Vision Transformers (ViTs) [8]. And it has been widely adopted in human mesh estimation [2, 6, 9, 18, 19, 43, 51]. For single-person settings, methods such as [6, 9, 18, 19, 51] focus on improving the accuracy through various architectural designs. Inspired by the DETR series [5, 23, 56] in object detection, recent methods have adopted a DETR-style framework for multi-person pose and mesh estimation [2, 22, 42, 43, 50], enabling one-stage estimation for all individuals. These works primarily focus on designing decoder queries to represent humans, keypoints, and mesh parameters. For instance, AiOS [43] refines predictions by progressively filtering and expanding queries in the decoder, while Multi-HMR [2] uses each query to represent a detected person. Our method also builds upon the DETR framework but focuses on improving token representations in the encoder to capture scale-aware human features, enabling accurate 3D mesh regression.

2.3. Efficient Vision Transformers

Although ViTs [8] achieves significant success across various vision tasks, their quadratic computational complexity remains a major challenge, particularly for tasks that require dense predictions such as object detection [46]. As a result, efforts to accelerate ViTs primarily focus on reducing the overall number of image tokens. For instance, [29, 36, 52] drop less informative tokens, [4, 38] merge similar tokens, and [40] proposes a mixed-resolution image tokenization scheme. Recently, TORE [9] accelerates single-person 3D mesh estimation by pruning background tokens. However, since background still provides important context, entirely discarding it leads to performance degradation (see Sec. 4.4). In this work, we propose a new perspective with scale-adaptive tokens that achieve a more effective trade-off between performance and computational cost.

3. Method

3.1. Preliminaries

We use SMPL [24] as our body model \mathcal{M} , which uses pose and shape parameters to represent the human body. Specifically, the pose parameters $\theta \in \mathbb{R}^{24 \times 3}$ are the relative rotations of 24 body joints, and the shape parameters $\beta \in \mathbb{R}^{10}$ describe the body shape. The model outputs a human mesh $\mathbf{V} = \mathcal{M}(\theta, \beta) \in \mathbb{R}^{6890 \times 3}$ and the 3D joints can be obtained via $\mathbf{J} = \mathbf{M}\mathbf{V} \in \mathbb{R}^{J \times 3}$, where $\mathbf{M} \in \mathbb{R}^{J \times 6890}$ is the joint regressor, and J represents the number of joints.

3.2. Overview

Building on recent methods [2, 43], we utilize a DETR-style pipeline [5], consisting of a Transformer encoder, decoder, and prediction heads for regressing SMPL parameters.

Naive baseline. While high-resolution inputs are shown to significantly enhance estimation accuracy [2, 43], they also introduce considerable computational overhead. To further explore the trade-off between resolution and efficiency, we first introduce a simple baseline using a similar architecture to [2], as depicted in Fig. 3 (top).

Given an RGB image $\mathbf{I}_{\text{hr}} \in \mathbb{R}^{H_{\text{hr}} \times W_{\text{hr}} \times 3}$, it is divided into regular patches of size $P \times P$. Patch embedding and positional embedding are then applied to these image patches, resulting in a sequence of image feature tokens $\mathcal{T} = \{t_1, t_2, \dots, t_k\}$, where $k = H_{\text{hr}}/P \times W_{\text{hr}}/P$. These tokens are subsequently processed by a Transformer encoder. In the decoder, a set of human queries is initialized as $\mathcal{Q} = \{q_1, q_2, \dots, q_n\}$, where n is a predefined hyperparameter large enough to detect all the individuals. After being processed by the decoder, these human queries are passed through multiple prediction heads: pose head \mathcal{H}_p , shape head \mathcal{H}_s , translation head \mathcal{H}_t , and box head \mathcal{H}_b to predict SMPL parameters (pose θ , shape β , and 3D translation \mathbf{t}) and bounding boxes, respectively. Each of the four

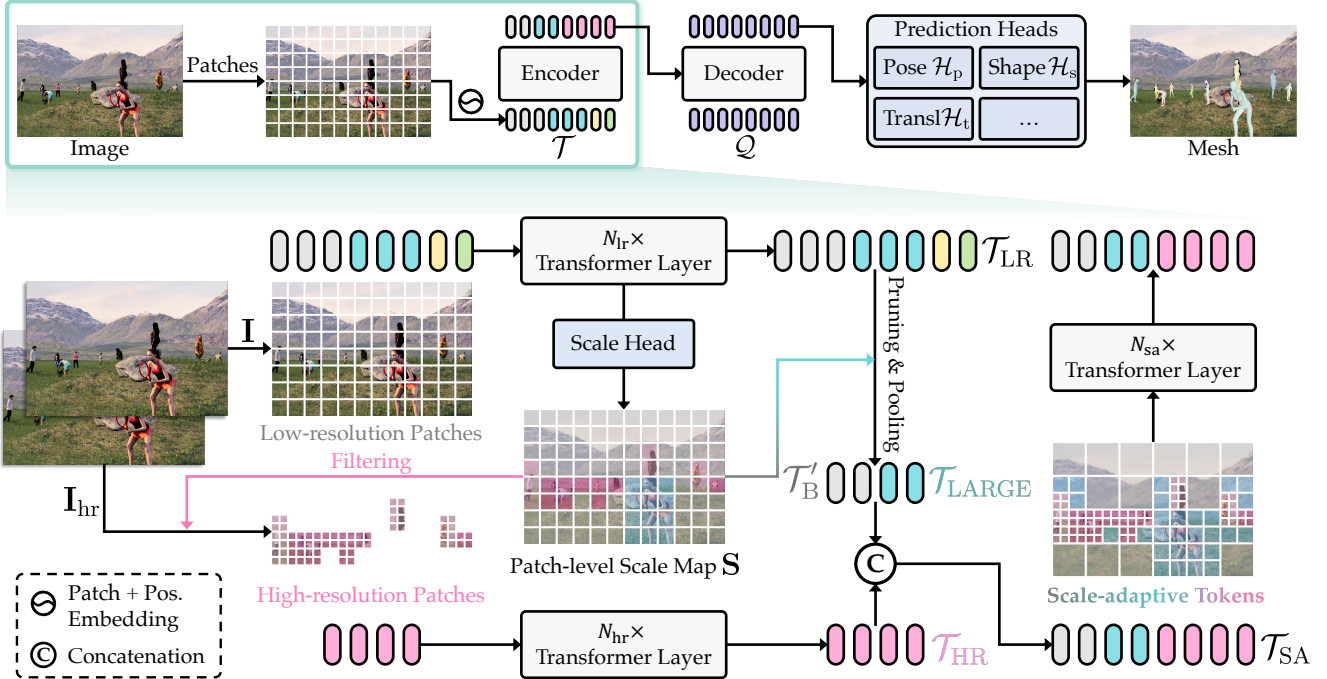


Figure 3. **Overview of (top) the baseline method and (bottom) our method with scale-adaptive tokens.** **Top:** Our baseline method adopts a DETR-style [5] pipeline consisting of a Transformer encoder, decoder, and prediction heads for regressing SMPL parameters. **Bottom:** Our method focuses on efficient feature encoding using scale-adaptive tokens. Specifically, low-resolution and high-resolution patches are extracted from the input images \mathbf{I} and \mathbf{I}_{hr} , respectively. A scale head network predicts a patch-level scale map \mathbf{S} from the low-resolution tokens, classifying them into three categories: background, small-scale, and large-scale. This scale map guides the pruning and pooling of low-resolution tokens \mathcal{T}_{LR} and indicates which patches should be replaced by high-resolution ones. By concatenating the pooled background tokens \mathcal{T}'_B , the remaining large-scale low-resolution tokens \mathcal{T}_{LARGE} , and the high-resolution tokens \mathcal{T}_{HR} , we obtain scale-adaptive tokens \mathcal{T}_{SA} . These tokens are then processed by the encoder, decoder, and multiple prediction heads to regress the human mesh.

prediction heads is implemented as an Multi-Layer Perceptron (MLP). Additionally, a linear projection is applied to the human queries to compute confidence scores, which are used to filter valid predictions with a threshold α_d .

Motivation. We evaluate the baseline with different image resolutions as input (see Fig. 2, Sec. 4.4 for details) and observe that high-resolution inputs significantly improve estimation accuracy, particularly for small-scale individuals whose size is relatively small to the image. However, for large-scale individuals, *e.g.*, those closer to the camera, the benefits of higher resolution are much less pronounced. Despite these improvements, high-resolution inputs bring a substantial increase in computational cost, which is consistent with findings from prior work [2, 43] (see Fig. 1).

This motivates us to explore more efficient strategies that balance performance and speed and we aim to encode the image feature more efficiently from an earlier stage. For large-scale individuals, additional tokens may be unnecessary; instead, computational resources should be allocated more effectively. To address this, we introduce **scale-adaptive tokens**, which replace the uniformly partitioned tokens used in the baseline. In the following sections, we will explain

how the scale is defined and computed, and how the tokens are adjusted accordingly (Sec. 3.3), followed by a discussion of the training process (Sec. 3.4).

3.3. Scale-Adaptive Tokens

As shown in Fig. 3 (bottom), we begin with a low-resolution image $\mathbf{I} \in \mathbb{R}^{H \times W \times 3}$, where $(H, W) = (H_{hr}/2, W_{hr}/2)$, and first uniformly partition it into low-resolution patches. Our goal is to adjust the resolution of each patch based on the scale of the individual it represents. To achieve this, we introduce a *patch-level scale map* that guides the resolution adjustments for each patch. Specifically, this map determines which low-resolution tokens should be further subdivided and replaced by high-resolution ones, and which tokens can be compressed. The high-resolution patches are extracted from a corresponding high-resolution image \mathbf{I}_{hr} . After being processed by the Transformer layers, the remaining low-resolution tokens and the newly generated high-resolution tokens are combined into *scale-adaptive tokens*, which provide a more efficient representation with varying levels of detail. These scale-adaptive tokens are then passed through additional Transformer layers and, finally, to the decoder to regress the SMPL parameters.

Patch-level scale map. We define a patch-level scale map $\mathbf{S} \in [0, 1]^{\frac{H}{P} \times \frac{W}{P} \times 2}$ for patches extracted from the low-resolution image \mathbf{I} . For each patch, the scale map $\mathbf{S}(i, j) = (c, s)$ contains two values: c represents the confidence indicating whether the patch overlaps with an individual, where 0 denotes the background; s represents the scale of the individual within the patch, defined as

$$s = \min(d_{\text{bb}}/S_{\text{hr}}, 1), \quad (1)$$

where d_{bb} is the diagonal length of the bounding box in \mathbf{I}_{hr} , and $S_{\text{hr}} = \max(H_{\text{hr}}, W_{\text{hr}})$. If the patch overlaps with multiple individuals, we use the scale of the individual closest to the camera, *i.e.*, the one with the smaller depth. The scale is only defined for patches overlapping with individuals, and for background patches, the scale value is ignored.

To predict the patch-level scale map, we pass the low-resolution patches through a shallow transformer encoder with N_{lr} layers, followed by a scale head network, implemented as an MLP. As illustrated in Fig. 3, patches without color are classified as background, while colored regions represent patches overlapping with individuals. A color gradient from blue to rose indicates the scale of the individuals, with blue representing large-scale individuals and rose representing small-scale individuals.

Scale-adaptive encoder. Building on the predicted scale map \mathbf{S} , the low-resolution tokens $\mathcal{T}_{\text{LR}} = \{t_1^{\text{lr}}, t_2^{\text{lr}}, \dots, t_{k_{\text{lr}}}^{\text{lr}}\}$ generated from the low-resolution patches are then classified into three groups: background \mathcal{T}_{B} , small-scale $\mathcal{T}_{\text{SMALL}}$, and large-scale $\mathcal{T}_{\text{LARGE}}$ tokens. Tokens identified as background, based on a confidence score c that meets a threshold α_c , are marked as background tokens $\mathcal{T}_{\text{B}} = \{t_1^{\text{b}}, t_2^{\text{b}}, \dots, t_{k_{\text{b}}}^{\text{b}}\}$. The remaining tokens are further categorized by their scale values s using a scale threshold α_s and are assigned to either the *small-scale* category, denoted by $\mathcal{T}_{\text{SMALL}} = \{t_1^{\text{small}}, t_2^{\text{small}}, \dots, t_{k_{\text{small}}}^{\text{small}}\}$, or the *large-scale* category, denoted by $\mathcal{T}_{\text{LARGE}} = \{t_1^{\text{large}}, t_2^{\text{large}}, \dots, t_{k_{\text{large}}}^{\text{large}}\}$.

Small-scale tokens are pruned and replaced by their high-resolution counterparts. High-resolution tokens are generated by applying a shallow transformer encoder with N_{hr} layers to the high-resolution image \mathbf{I}_{hr} , where $N_{\text{hr}} = N_{\text{lr}}$ to ensure feature alignment. The small-scale tokens are then replaced by their corresponding high-resolution tokens (Fig. 3), resulting in an expanded set of high-resolution tokens, denoted as $\mathcal{T}_{\text{HR}} = \{t_1^{\text{hr}}, t_2^{\text{hr}}, \dots, t_{k_{\text{hr}}}^{\text{hr}}\}$, where $k_{\text{hr}} = 4k_{\text{small}}$.

Although background can provide valuable contextual information, their feature encoding can be further optimized. To this end, we distill the background tokens \mathcal{T}_{B} by spatially pooling every four neighboring tokens, resulting in pooled background tokens $\mathcal{T}'_{\text{B}} = \{t_1^{\text{b}'}, t_2^{\text{b}'}, \dots, t_{k_{\text{b}'}}^{\text{b}'}\}$. To avoid irregular pooling, some low-resolution tokens that cannot be grouped remain unchanged. As a result, $k_{\text{b}'}$ does not necessarily equal $k_{\text{b}}/4$. By retaining these tokens, we bet-

ter preserve their positional information, which facilitates subsequent positional encoding operations [23].

The remaining tokens in \mathcal{T}_{LR} representing large-scale individuals, $\mathcal{T}_{\text{LARGE}}$, remain unchanged. Next, we integrate the different tokens, including pooled background tokens and high-resolution tokens from selected regions. This results in scale-adaptive tokens, denoted as $\mathcal{T}_{\text{SA}} = \{\mathcal{T}'_{\text{B}}, \mathcal{T}_{\text{LARGE}}, \mathcal{T}_{\text{HR}}\}$. Compared to the uniform low-resolution tokens, this approach allocates feature details more efficiently, preserving different levels of detail for different individuals and regions.

These tokens, \mathcal{T}_{SA} , are then processed by another Transformer encoder with N_{sa} layers and further decoded in subsequent stages. Fig. 3 (bottom) provides an overview of the scale-adaptive encoder.

Decoder and prediction heads. The decoder and prediction heads follow the architecture of our baseline approach as mentioned in Sec. 3.2. For detailed architectures, please refer to the supplementary material (Sec. A.1).

3.4. Training Losses

Similar to DETR [5], we first match our human predictions to ground-truth (GT) using Hungarian Matching, and we leverage bounding boxes, confidence scores, and projected joints during the matching. This matching step is necessary before computing the overall loss \mathcal{L} . More details on the matching process are provided in Sec. A.1. The loss function, \mathcal{L} , is a weighted sum of various terms, with each λ representing a hyperparameter:

$$\begin{aligned} \mathcal{L} = & \lambda_{\text{map}} \mathcal{L}_{\text{map}} + \lambda_{\text{depth}} \mathcal{L}_{\text{depth}} + \lambda_{\text{pose}} \mathcal{L}_{\text{pose}} + \lambda_{\text{shape}} \mathcal{L}_{\text{shape}} \\ & + \lambda_{\text{j3d}} \mathcal{L}_{\text{j3d}} + \lambda_{\text{j2d}} \mathcal{L}_{\text{j2d}} + \lambda_{\text{box}} \mathcal{L}_{\text{box}} + \lambda_{\text{det}} \mathcal{L}_{\text{det}}. \end{aligned}$$

Scale map loss \mathcal{L}_{map} . To supervise the patch-level scale map, we apply focal loss [21] to the predicted confidence c and L1 loss to the predicted scale s . The total loss, \mathcal{L}_{map} , is the sum of these two terms. The GT for confidence and scale is precomputed, as described in Sec. 3.3.

Depth loss $\mathcal{L}_{\text{depth}}$. We supervise the root depth (*i.e.*, the z-dimension) of the 3D joints \mathbf{J} , regressed from the predicted mesh \mathbf{V} (Sec. 3.1). Specifically, we normalize the depth based on the focal length, following [10]. The depth loss is calculated as $\mathcal{L}_{\text{depth}} = \left| \frac{1}{\tilde{d}} - \frac{f}{\tilde{f}d} \right|$, where f is the predefined focal length of our camera, and \tilde{d} and \tilde{f} are the GT depth and focal length, respectively. See Sec. A.1 for more details.

Other losses. For the pose parameters loss $\mathcal{L}_{\text{pose}}$, shape parameters loss $\mathcal{L}_{\text{shape}}$, 3D joints loss \mathcal{L}_{j3d} , and projected 2D joints loss \mathcal{L}_{j2d} , we use the L1 distance. For the bounding box loss \mathcal{L}_{box} , we combine L1 loss with GIoU loss [39]. The detection loss \mathcal{L}_{det} uses focal loss [21] to supervise the confidence scores of human queries.

Table 1. **Comparison with SOTA methods on AGORA test set [32].** “Res.” represents the input resolution. “644*” means we use a base resolution of 644 and adaptively scale certain regions up to a maximum resolution of 1288.

| Method | Res. | Time (ms) | MACs (G) | F1-Score \uparrow | Precision \uparrow | Recall \uparrow | MPJPE \downarrow | MVE \downarrow | NMJE \downarrow | NMVE \downarrow |
|---------------|------|-----------|----------|---------------------|----------------------|-------------------|--------------------|------------------|-------------------|-------------------|
| ROMP [44] | 512 | 38.7 | 43.6 | 0.91 | 0.95 | 0.88 | 108.1 | 103.4 | 118.8 | 113.6 |
| BEV [45] | 512 | 50.6 | 48.9 | 0.93 | 0.96 | 0.90 | 105.3 | 100.7 | 113.2 | 108.3 |
| PSVT [35] | 512 | - | - | 0.93 | - | - | 97.7 | 94.1 | 105.1 | 101.2 |
| AiOS [43] | 1333 | 405.2 | 314.5 | 0.94 | 0.98 | 0.90 | 63.9 | 57.5 | 68.0 | 61.2 |
| Multi-HMR [2] | 896 | 97.4 | 2075.1 | 0.93 | - | - | 82.8 | 77.6 | 89.0 | 83.4 |
| Multi-HMR [2] | 1288 | 231.7 | 6104.6 | 0.95 | 0.97 | 0.93 | 65.3 | 61.1 | 68.7 | 64.3 |
| Ours | 644* | 42.0 | 133.1 | 0.95 | 0.98 | 0.91 | 67.9 | 63.3 | 71.5 | 66.6 |

4. Experiments

4.1. Datasets and metrics

We train our model on multi-person datasets including AGORA [32], BEDLAM [3], COCO [20], Crowdpose [17], and MPII [1], as well as the single-person dataset H3.6M [13]. AGORA and BEDLAM are synthetic datasets with high-quality 3D mesh GTs. For other multi-person datasets, we use pseudo GTs from NeuralAnnot [30] and only supervise projected 2D joints.

For comparison with SOTA methods, we evaluate our method on AGORA [32], MuPoTS [28], 3DPW [48], and CMU Panoptic [15] datasets. Following previous works [2, 43–45], we report Mean Vertex Error (MVE) and Mean Per-Joint Position Error (MPJPE) before and after Procrustes-Alignment (PA). On AGORA, we also report F1-Score, precision, and recall for evaluating detection accuracy; Normalized Mean Vertex Error (NMVE) and Normalized Mean Joint Error (NMJE) that considered regression accuracy with detection accuracy. All metrics above, except detection accuracy, are reported in millimeters (mm). On MuPoTS-3D [28], we report the Percentage of Correctly estimated Keypoints (PCK) using a threshold of 15 cm. To evaluate computational costs, we report Multiply-Add Cumulation (MACs) and the average inference time (ms) following [2] on one RTX 3090 GPU.

4.2. Implementation Details

The input image is resized to maintain its original aspect ratio, with a base resolution of $\max(H, W) = 644$ and $\max(H_{hr}, W_{hr}) = 1288$ for high-resolution when needed. We denote this mixed-resolution setting as “644*”. The Transformer layers in our encoder are initialized using pre-trained DINOv2 [31] with ViT-B architecture and a patch size of $P = 14$. The Transformer used in the encoder has $N_r = N_{hr} = 3$, and $N_{sa} = 9$ layers, respectively. Our decoder consists of 6 Transformer layers and 50 human queries. Training is conducted on 8 RTX 3090 GPUs with a total batch size of 40 for 60 epochs with an initial learning rate of $4e - 5$. Please refer to Sec. A.2 for more details.

Table 2. **Comparison with SOTA methods on 3DPW [48] and MuPoTS [28] test sets.** “Res.” represents the input resolution. “Crop” refers to cropping individuals for single-person mesh estimation, *i.e.*, a multi-stage approach. “644*” means a base resolution of 644, with adaptive scaling up to 1288.

| Method | Res. | 3DPW | | MuPoTS (PCK) | |
|----------------|------|-----------------------|------------------|----------------|--------------------|
| | | PA-MPJPE \downarrow | MVE \downarrow | All \uparrow | Matched \uparrow |
| CRMH [14] | 832 | - | - | 69.1 | 72.2 |
| 3DCrowdNet [7] | Crop | 51.5 | 98.3 | 72.7 | 73.3 |
| ROMP [44] | 512 | 47.3 | 93.4 | 69.9 | 72.2 |
| BEV [45] | 512 | 46.9 | 92.3 | 70.2 | 75.2 |
| PSVT [35] | 512 | 45.7 | 84.9 | - | - |
| Multi-HMR [2] | 896 | 41.7 | 75.9 | 85.0 | 89.3 |
| Ours | 644* | 41.6 | 73.7 | 89.0 | 90.1 |

4.3. Comparison to the State-of-the-arts

Performance and Efficiency. We conduct evaluations on the AGORA [32], 3DPW [48], MuPoTS [27], and CMU Panoptic [15] datasets. Tab. 1 shows the results of our method compared to SOTA methods on the AGORA [32] test set leaderboard. Our method, using a mixed resolution input with a base of 644, achieves performance on par with the top SOTA methods [2, 43], despite their use of higher resolutions and larger models (*e.g.*, Multi-HMR use ViT-L [31] model). These methods, however, result in significantly higher computational complexity, including much higher MACs and slower runtime, compromising real-time performance. Besides, these methods [2, 43] estimates SMPL-X [33], from which SMPL [24] mesh is derived. In contrast, our method maintains real-time computational efficiency while improving upon real-time methods ROMP [44], by nearly 40%. This establishes our approach as **the leading real-time model**, setting a new standard by achieving **an unparalleled balance of performance and efficiency**.

Tab. 2 presents the results of our method on the 3DPW dataset. Following Multi-HMR [2], we finetune on the 3DPW training set. We further evaluate the generalization performance of our method on the MuPoTS and CMU Panoptic datasets, as shown in Tab. 2 and Tab. 3. For Panoptic dataset, we follow the common evaluation protocol



Figure 4. **Comparison with SOTA methods [2, 43–45] on in-the-wild images from the Internet.** Red dashed circles highlight areas with incorrect estimations. The third case is left blank due to the small scale of individuals. Please zoom in for details.

Table 3. **Comparison with SOTA methods on CMU Panoptic [15] test set.** We report MPJPE for four activities and the average.

| Method | Hagglng ↓ | Mafia ↓ | Ultimatum ↓ | Pizza ↓ | Avg. ↓ |
|----------------|-------------|-------------|-------------|-------------|-------------|
| CRMH [14] | 129.6 | 133.5 | 153.0 | 156.7 | 143.2 |
| 3DCrowdNet [7] | 109.6 | 135.9 | 129.8 | 135.6 | 127.6 |
| ROMP [44] | 110.8 | 122.8 | 141.6 | 137.6 | 128.2 |
| BEV [45] | 90.7 | 103.7 | 113.1 | 125.2 | 109.5 |
| PSVT [35] | 88.7 | 97.9 | 115.2 | 121.2 | 105.7 |
| Ours | 67.9 | 78.5 | 95.8 | 94.6 | 84.2 |

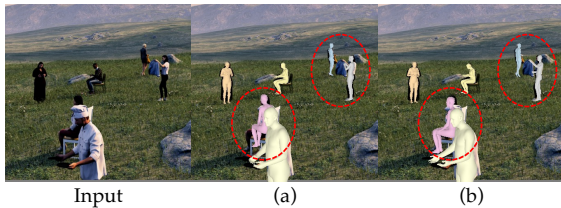


Figure 5. **Qualitative comparison of different resolutions for our baseline.** Resolution for the baseline: (a) 518, (b) 1288. Red dashed circles highlight differences; zoom in for details.

[35, 44, 45] and exclude Multi-HMR [2] due to potential inconsistencies in joint format. Our method consistently achieves the best results across all datasets, demonstrating exceptional generalization capability.

Qualitative Results. Fig. 4 presents a visual comparison between our method and existing SOTA approaches. The images are sourced from the Internet. Our method provides the most accurate overall estimations, especially in the third case, where individuals are far from the camera, resulting in very small scales. Despite this challenge, our method remains highly **robust**, delivering precise estimations. In contrast, ROMP [44] and BEV [45] fail to detect all individuals, while AiOS [43] and Multi-HMR [2], despite using higher-resolution models, show significant estimation errors.

Table 4. **Ablation studies on BEDLAM [3] validation set.** We report MVE for different scale ranges and the average (Avg.).

| Ablation | 0-20% | 20-40% | 40-60% | 60-80% | 80%+ | Avg. |
|-----------------|-------|--------|--------|--------|------|------|
| (a) Drop all | 59.9 | 55.1 | 61.5 | 66.6 | 70.8 | 57.2 |
| (b) No pooling | 60.3 | 54.5 | 57.0 | 59.8 | 64.1 | 56.1 |
| (c) Pooling × 2 | 60.7 | 54.5 | 57.5 | 62.1 | 66.5 | 56.3 |
| (d) Ours | 60.0 | 54.4 | 57.2 | 60.3 | 62.7 | 56.0 |

4.4. Ablation Study

We conduct ablation studies using only the AGORA [32] and sampled BEDLAM [3] datasets to validate model designs, and report results on their validation sets.

Impact of resolution. Fig. 2 shows baseline results with different input resolutions on the AGORA [32] validation set. As resolution increases, the error across individuals in different scale ranges consistently decreases, with the most significant drop (35mm) in the smallest scale range. In contrast, the improvement in the large-scale range is less pronounced. However, the performance gain comes at the cost of a significant drop in computational efficiency, reducing the frame rate from real-time (32 FPS) to 5 FPS. Fig. 5 shows an example, clearly illustrating that higher resolution greatly improves estimation for small-scale individuals.

Background tokens \mathcal{T}_B . We investigate the impact of background tokens on model performance and report the MVE across different scale ranges on the BEDLAM validation set in Tab. 4. In (a), we discard all background tokens and observe stable performance at the smallest scale, but a decline as the scale increases, indicating that background context becomes more important for larger scales. In (b), skipping pooling for background tokens yields nearly the same performance but introduces higher computational cost. In (c), applying pooling twice with the same grouping strategy results in a performance drop for large-scale instances, highlighting the significance of background context for es-

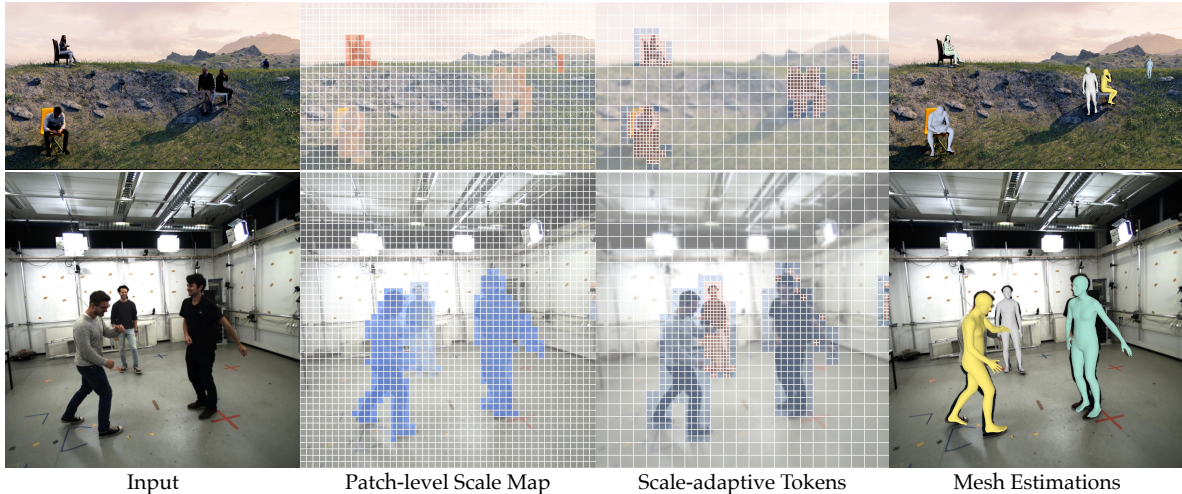


Figure 6. **Visualization of our predicted patch-level scale maps S and scale-adaptive tokens T_{SA} .** We show the predicted scale maps, scale-adaptive tokens, and the estimated meshes overlaid on the image. In the scale map, colors represent scale values, with uncolored areas indicating background patches. A gradient from blue (large-scale individuals) to pink (small-scale individuals) illustrates the scale distribution. We visualize scale-adaptive tokens as patches of different sizes and colors on the image, with low-resolution patches blurred.

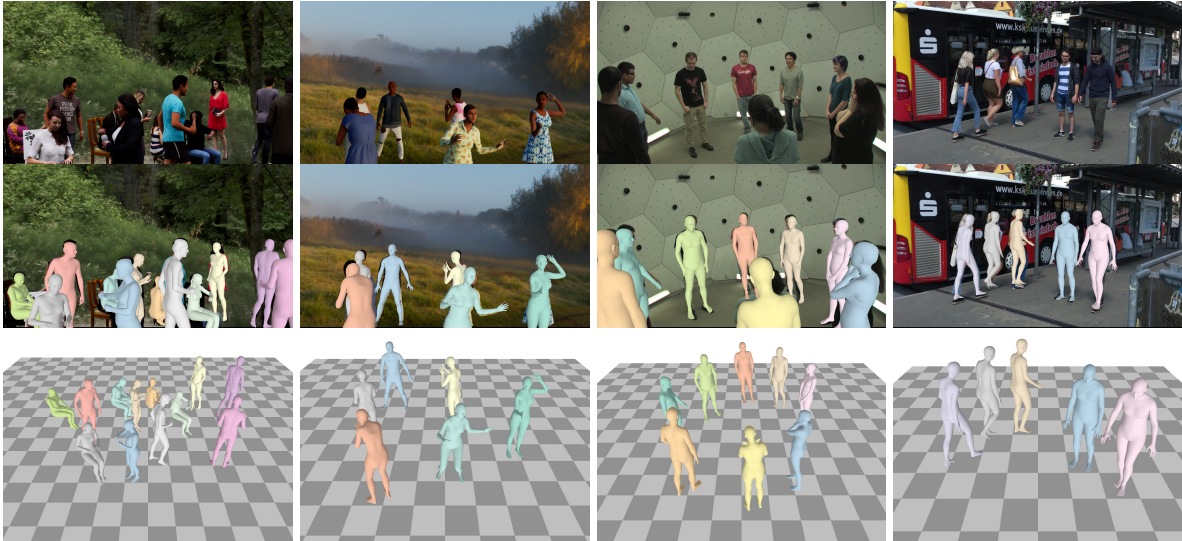


Figure 7. **Qualitative results of our method.** We visualize four cases from AGORA [32], BEDLAM [3], CMU Panoptic [15] and 3DPW [48] datasets, displaying the input, the estimated mesh overlay, and an elevated view (top to bottom).

timation. We provide additional efficiency comparisons in Sec. B, showing that pooling once achieves the best balance between performance and efficiency.

4.5. Qualitative Results

Fig. 6 visualize the predicted patch-level scale map and scale-adaptive tokens by our model, enabling dynamic adjustment of tokens for accurate estimations. Fig. 7 presents additional visualizations of predicted meshes, demonstrating the effectiveness of our method in various scenarios. Please refer to Sec. B for more qualitative results and discussion.

5. Conclusion

We present a novel one-stage framework for real-time multi-person 3D mesh estimation from an RGB image. By introducing scale-adaptive tokens that dynamically adjust based on the relative scale of individuals, our method effectively balances efficiency and accuracy, retaining the benefits of high-resolution processing while achieving real-time performance. Experiments demonstrate that our method is the **best real-time model**, offering competitive performance and superior generalization compared to SOTAs. Our **limitations** include the lack of height-aware scale estimation, which may cause depth errors, and the current focus on body-only mesh estimation, extendable to whole-body in the future.

References

- [1] Mykhaylo Andriluka, Leonid Pishchulin, Peter Gehler, and Bernt Schiele. 2d human pose estimation: New benchmark and state of the art analysis. In *CVPR*, pages 3686–3693, 2014. 6, 1
- [2] Fabien Baradel, Matthieu Armando, Salma Galaoui, Romain Brégier, Philippe Weinzaepfel, Grégory Rogez, and Thomas Lucas. Multi-hmr: Multi-person whole-body human mesh recovery in a single shot. In *ECCV*, 2024. 2, 3, 4, 6, 7, 1, 5
- [3] Michael J Black, Priyanka Patel, Joachim Tesch, and Jinlong Yang. Bedlam: A synthetic dataset of bodies exhibiting detailed lifelike animated motion. In *CVPR*, pages 8726–8737, 2023. 6, 7, 8, 1, 2, 3, 4
- [4] Daniel Bolya, Cheng-Yang Fu, Xiaoliang Dai, Peizhao Zhang, Christoph Feichtenhofer, and Judy Hoffman. Token merging: Your ViT but faster. In *ICLR*, 2023. 3
- [5] Nicolas Carion, Francisco Massa, Gabriel Synnaeve, Nicolas Usunier, Alexander Kirillov, and Sergey Zagoruyko. End-to-end object detection with transformers. In *ECCV*, pages 213–229. Springer, 2020. 2, 3, 4, 5, 1
- [6] Junhyeong Cho, Kim Youwang, and Tae-Hyun Oh. Cross-attention of disentangled modalities for 3d human mesh recovery with transformers. In *ECCV*, 2022. 3
- [7] Hongsuk Choi, Gyeongsik Moon, JoonKyu Park, and Kyoung Mu Lee. Learning to estimate robust 3d human mesh from in-the-wild crowded scenes. In *CVPR*, pages 1475–1484, 2022. 2, 3, 6, 7
- [8] Alexey Dosovitskiy, Lucas Beyer, Alexander Kolesnikov, Dirk Weissenborn, Xiaohua Zhai, Thomas Unterthiner, Mostafa Dehghani, Matthias Minderer, Georg Heigold, Sylvain Gelly, Jakob Uszkoreit, and Neil Houlsby. An image is worth 16x16 words: Transformers for image recognition at scale. In *ICLR*, 2021. 3
- [9] Zhiyang Dou, Qingxuan Wu, Cheng Lin, Zeyu Cao, Qiangqiang Wu, Weilin Wan, Taku Komura, and Wenping Wang. Tore: Token reduction for efficient human mesh recovery with transformer. In *ICCV*, pages 15143–15155, 2023. 3
- [10] Jose M Facil, Benjamin Ummenhofer, Huizhong Zhou, Luis Montesano, Thomas Brox, and Javier Civera. Cam-convs: Camera-aware multi-scale convolutions for single-view depth. In *CVPR*, pages 11826–11835, 2019. 5
- [11] Shubham Goel, Georgios Pavlakos, Jathushan Rajasegaran, Angjoo Kanazawa, and Jitendra Malik. Humans in 4d: Reconstructing and tracking humans with transformers. In *ICCV*, pages 14783–14794, 2023. 3, 1
- [12] Kaiming He, Xiangyu Zhang, Shaoqing Ren, and Jian Sun. Deep residual learning for image recognition. In *CVPR*, pages 770–778, 2016. 3
- [13] Catalin Ionescu, Dragos Papava, Vlad Olaru, and Cristian Sminchisescu. Human3.6m: Large scale datasets and predictive methods for 3d human sensing in natural environments. *IEEE TPAMI*, 36(7):1325–1339, 2013. 6, 1
- [14] Wen Jiang, Nikos Kolotouros, Georgios Pavlakos, Xiaowei Zhou, and Kostas Daniilidis. Coherent reconstruction of multiple humans from a single image. In *CVPR*, pages 5579–5588, 2020. 2, 3, 6, 7
- [15] Hanbyul Joo, Hao Liu, Lei Tan, Lin Gui, Bart Nabbe, Iain Matthews, Takeo Kanade, Shohei Nobuhara, and Yaser Sheikh. Panoptic studio: A massively multiview system for social motion capture. In *ICCV*, pages 3334–3342, 2015. 6, 7, 8, 2
- [16] Nikos Kolotouros, Georgios Pavlakos, Michael J Black, and Kostas Daniilidis. Learning to reconstruct 3d human pose and shape via model-fitting in the loop. In *ICCV*, pages 2252–2261, 2019. 1
- [17] Jiefeng Li, Can Wang, Hao Zhu, Yihuan Mao, Hao-Shu Fang, and Cewu Lu. Crowdpose: Efficient crowded scenes pose estimation and a new benchmark. In *CVPR*, pages 10863–10872, 2019. 6, 1
- [18] Kevin Lin, Lijuan Wang, and Zicheng Liu. End-to-end human pose and mesh reconstruction with transformers. In *CVPR*, pages 1954–1963, 2021. 3
- [19] Kevin Lin, Lijuan Wang, and Zicheng Liu. Mesh graphormer. In *ICCV*, pages 12939–12948, 2021. 3
- [20] Tsung-Yi Lin, Michael Maire, Serge Belongie, James Hays, Pietro Perona, Deva Ramanan, Piotr Dollár, and C Lawrence Zitnick. Microsoft coco: Common objects in context. In *ECCV*, pages 740–755, 2014. 6, 1
- [21] Tsung-Yi Lin, Priya Goyal, Ross Girshick, Kaiming He, and Piotr Dollár. Focal loss for dense object detection. In *ICCV*, 2017. 5
- [22] Huan Liu, Qiang Chen, Zichang Tan, Jiang-Jiang Liu, Jian Wang, Xiangbo Su, Xiaolong Li, Kun Yao, Junyu Han, Errui Ding, et al. Group pose: A simple baseline for end-to-end multi-person pose estimation. In *ICCV*, pages 15029–15038, 2023. 3
- [23] Shilong Liu, Feng Li, Hao Zhang, Xiao Yang, Xianbiao Qi, Hang Su, Jun Zhu, and Lei Zhang. DAB-DETR: Dynamic anchor boxes are better queries for DETR. In *ICLR*, 2022. 3, 5, 1, 2
- [24] Matthew Loper, Naureen Mahmood, Javier Romero, Gerard Pons-Moll, and Michael J Black. Smpl: A skinned multi-person linear model. *ACM TOG*, 34(6):1–16, 2015. 1, 3, 6
- [25] Ilya Loshchilov and Frank Hutter. Decoupled weight decay regularization. In *ICLR*, 2017. 1
- [26] Xiaoxuan Ma, Jiajun Su, Chunyu Wang, Wentao Zhu, and Yizhou Wang. 3d human mesh estimation from virtual markers. In *CVPR*, pages 534–543, 2023. 3
- [27] Dushyant Mehta, Helge Rhodin, Dan Casas, Pascal Fua, Oleksandr Sotnychenko, Weipeng Xu, and Christian Theobalt. Monocular 3d human pose estimation in the wild using improved cnn supervision. In *3DV*, pages 506–516, 2017. 6
- [28] Dushyant Mehta, Oleksandr Sotnychenko, Franziska Mueller, Weipeng Xu, Srinath Sridhar, Gerard Pons-Moll, and Christian Theobalt. Single-shot multi-person 3d pose estimation from monocular rgb. In *3DV*, pages 120–130, 2018. 6, 1
- [29] Lingchen Meng, Hengduo Li, Bor-Chun Chen, Shiyi Lan, Zuxuan Wu, Yu-Gang Jiang, and Ser-Nam Lim. Advait: Adaptive vision transformers for efficient image recognition. In *CVPR*, pages 12309–12318, 2022. 3
- [30] Gyeongsik Moon, Hongsuk Choi, and Kyoung Mu Lee. Neuralannot: Neural annotator for 3d human mesh training sets. In *CVPR*, pages 2299–2307, 2022. 6, 1

- [31] Maxime Oquab, Timothée Darcet, Théo Moutakanni, Huy V Vo, Marc Szafranec, Vasil Khalidov, Pierre Fernandez, Daniel HAZIZA, Francisco Massa, Alaaeldin El-Nouby, et al. Dinov2: Learning robust visual features without supervision. *Transactions on Machine Learning Research*, 2024. 6
- [32] Priyanka Patel, Chun-Hao P Huang, Joachim Tesch, David T Hoffmann, Shashank Tripathi, and Michael J Black. Agora: Avatars in geography optimized for regression analysis. In *CVPR*, pages 13468–13478, 2021. 1, 2, 6, 7, 8, 3, 4
- [33] Georgios Pavlakos, Vasileios Choutas, Nima Ghorbani, Timo Bolkart, Ahmed AA Osman, Dimitrios Tzionas, and Michael J Black. Expressive body capture: 3d hands, face, and body from a single image. In *CVPR*, pages 10975–10985, 2019. 3, 6, 1
- [34] Zhongwei Qiu, Qiansheng Yang, Jian Wang, and Dongmei Fu. Dynamic graph reasoning for multi-person 3d pose estimation. In *Proceedings of the 30th ACM International Conference on Multimedia*, pages 3521–3529, 2022. 2, 3
- [35] Zhongwei Qiu, Qiansheng Yang, Jian Wang, Haocheng Feng, Junyu Han, Errui Ding, Chang Xu, Dongmei Fu, and Jingdong Wang. Psvt: End-to-end multi-person 3d pose and shape estimation with progressive video transformers. In *CVPR*, pages 21254–21263, 2023. 3, 6, 7
- [36] Yongming Rao, Wenliang Zhao, Benlin Liu, Jiwen Lu, Jie Zhou, and Cho-Jui Hsieh. Dynamicvit: Efficient vision transformers with dynamic token sparsification. In *NeurIPS*, pages 13937–13949, 2021. 3
- [37] Shaoqing Ren, Kaiming He, Ross Girshick, and Jian Sun. Faster R-CNN: Towards real-time object detection with region proposal networks. In *NeurIPS*, 2015. 3
- [38] Cedric Renggli, André Susano Pinto, Neil Houlsby, Basil Mustafa, Joan Puigcerver, and Carlos Riquelme. Learning to merge tokens in vision transformers. *arXiv preprint arXiv:2202.12015*, 2022. 3
- [39] Hamid Rezaatoughi, Nathan Tsoi, JunYoung Gwak, Amir Sadeghian, Ian Reid, and Silvio Savarese. Generalized intersection over union: A metric and a loss for bounding box regression. In *CVPR*, pages 658–666, 2019. 5
- [40] Tomer Ronen, Omer Levy, and Avram Golbert. Vision transformers with mixed-resolution tokenization. In *CVPRW*, pages 4613–4622, 2023. 3
- [41] Tim Salzmann, Hao-Tien Lewis Chiang, Markus Ryll, Dorsa Sadigh, Carolina Parada, and Alex Bewley. Robots that can see: Leveraging human pose for trajectory prediction. *IEEE Robotics and Automation Letters*, 2023. 2
- [42] Dahu Shi, Xing Wei, Liangqi Li, Ye Ren, and Wenming Tan. End-to-end multi-person pose estimation with transformers. In *CVPR*, pages 11069–11078, 2022. 3
- [43] Qingping Sun, Yanjun Wang, Ailing Zeng, Wanqi Yin, Chen Wei, Wenjia Wang, Haiyi Mei, Chi-Sing Leung, Ziwei Liu, Lei Yang, et al. Aios: All-in-one-stage expressive human pose and shape estimation. In *CVPR*, pages 1834–1843, 2024. 2, 3, 4, 6, 7, 1, 5
- [44] Yu Sun, Qian Bao, Wu Liu, Yili Fu, Michael J Black, and Tao Mei. Monocular, one-stage, regression of multiple 3d people. In *ICCV*, pages 11179–11188, 2021. 3, 6, 7, 1, 2
- [45] Yu Sun, Wu Liu, Qian Bao, Yili Fu, Tao Mei, and Michael J Black. Putting people in their place: Monocular regression of 3d people in depth. In *CVPR*, pages 13243–13252, 2022. 2, 3, 6, 7, 1, 5
- [46] Shitao Tang, Jiahui Zhang, Siyu Zhu, and Ping Tan. Quadtree attention for vision transformers. In *ICLR*, 2022. 3
- [47] A Vaswani. Attention is all you need. *NeurIPS*, 2017. 3
- [48] Timo von Marcard, Roberto Henschel, Michael J Black, Bodo Rosenhahn, and Gerard Pons-Moll. Recovering accurate 3d human pose in the wild using imus and a moving camera. In *ECCV*, pages 601–617, 2018. 1, 6, 8, 3
- [49] Yuan Xu, Xiaoxuan Ma, Jiajun Su, Wentao Zhu, Yu Qiao, and Yizhou Wang. Scorehypo: Probabilistic human mesh estimation with hypothesis scoring. In *CVPR*, pages 979–989, 2024. 3
- [50] Jie Yang, Ailing Zeng, Shilong Liu, Feng Li, Ruimao Zhang, and Lei Zhang. Explicit box detection unifies end-to-end multi-person pose estimation. In *ICLR*, 2023. 3
- [51] Sen Yang, Wen Heng, Gang Liu, Guozhong Luo, Wankou Yang, and YU Gang. Capturing the motion of every joint: 3d human pose and shape estimation with independent tokens. In *ICLR*, 2023. 3
- [52] Hongxu Yin, Arash Vahdat, Jose M Alvarez, Arun Mallya, Jan Kautz, and Pavlo Molchanov. A-vit: Adaptive tokens for efficient vision transformer. In *CVPR*, pages 10809–10818, 2022. 3
- [53] Andrei Zanfir, Elisabeta Marinoiu, and Cristian Sminchisescu. Monocular 3d pose and shape estimation of multiple people in natural scenes—the importance of multiple scene constraints. In *CVPR*, pages 2148–2157, 2018. 2, 3
- [54] Andrei Zanfir, Elisabeta Marinoiu, Mihai Zanfir, Alin-Ionut Popa, and Cristian Sminchisescu. Deep network for the integrated 3d sensing of multiple people in natural images. In *NeurIPS*, 2018. 2, 3
- [55] Hongwen Zhang, Yating Tian, Xinchu Zhou, Wanli Ouyang, Yebin Liu, Limin Wang, and Zhenan Sun. Pymaf: 3d human pose and shape regression with pyramidal mesh alignment feedback loop. In *ICCV*, pages 11446–11456, 2021. 3
- [56] Hao Zhang, Feng Li, Shilong Liu, Lei Zhang, Hang Su, Jun Zhu, Lionel Ni, and Heung-Yeung Shum. Dino: Detr with improved denoising anchor boxes for end-to-end object detection. In *ICLR*, 2023. 3
- [57] Wentao Zhu, Xiaoxuan Ma, Zhaoyang Liu, Libin Liu, Wayne Wu, and Yizhou Wang. Motionbert: A unified perspective on learning human motion representations. In *CVPR*, pages 15085–15099, 2023. 3
- [58] Wentao Zhu, Jason Qin, Yuke Lou, Hang Ye, Xiaoxuan Ma, Hai Ci, and Yizhou Wang. Social motion prediction with cognitive hierarchies. In *NeurIPS*, 2023. 2
- [59] Wentao Zhu, Xiaoxuan Ma, Dongwoo Ro, Hai Ci, Jinlu Zhang, Jiabin Shi, Feng Gao, Qi Tian, and Yizhou Wang. Human motion generation: A survey. *IEEE TPAMI*, 46(4): 2430–2449, 2024. 2

SAT-HMR: Real-Time Multi-Person 3D Mesh Estimation via Scale-Adaptive Tokens

Supplementary Material

In Sec. A.1, we elaborate on the implementation details of our proposed method and the experimental setups. We provide additional results and extended discussions in Sec. B.

A. Implementation Details

A.1. Model Architecture

Encoder-decoder design. Our model follows an encoder-decoder design based on previous works [2, 23], with the vanilla encoder replaced by our proposed scale-adaptive encoder. For the decoder, following [23], human queries consist of two learnable components: the *content* part and the *positional* part, also known as *decoder embeddings* and *anchor boxes* [23]. Following [23], anchor boxes are refined layer-by-layer by predicting residual values via a prediction head. Additionally, we initialize mean SMPL pose and shape parameters used in [2, 11, 16] and update them with a similar procedure, as illustrated in Fig. A1. Predictions of 3D translation t are regressed from updated decoder embeddings without iteratively updating, which is not included in Fig. A1. Finally, all human predictions are matched to GTs before computing training losses. We adopt the Hungarian algorithm following previous works [5, 43]. The matching cost is computed as a weighted sum of \mathcal{L}_{box} , \mathcal{L}_{det} , and \mathcal{L}_{j2d} , with the weights sharing the same values as those in Sec. A.2.

Camera model. To leverage 2D annotations for supervision, we adopt a pinhole camera model to project 3D joints onto the image plane. Given the focal length f and principal point (p_u, p_v) , a 3D point (x, y, z) is projected to the image coordinates (u, v) as follows:

$$u = \frac{f \times x}{z} + p_u, \quad v = \frac{f \times y}{z} + p_v. \quad (\text{A1})$$

Following [2, 45], we assume a standard camera with a fixed field of view (FOV) of 60° . Given S_{hr} as the longer side of the image, the focal length is predefined as $f = S_{\text{hr}} / (2 \tan(\text{FOV}/2))$. The principal point (p_u, p_v) is located at the center of the image.

A.2. Training

The confidence and scale thresholds corresponding to the scale map are set to $\alpha_c = 0.3$ and $\alpha_s = 0.5$, respectively. The loss weights are set to $\lambda_{\text{map}} = 4$, $\lambda_{\text{depth}} = 0.5$, $\lambda_{\text{pose}} = 5$, $\lambda_{\text{shape}} = 3$, $\lambda_{\text{j3d}} = 8$, $\lambda_{\text{j2d}} = 40$, $\lambda_{\text{box}} = 2$ and $\lambda_{\text{det}} = 4$. We train our model with AdamW [25], with weight decay set to $1e-4$. The initial learning rate for the pretrained parameters is set to $2e-5$, while for other parameters, it is set to $4e-5$.

The model is trained for 60 epochs with a total batch size of 40, which takes around a week on 8 RTX 3090 GPUs.

A.3. Datasets

We briefly introduce the datasets used for training or evaluation.

AGORA [32] is a synthetic dataset known for its high realism and diverse scenarios. Due to its highly accurate GTs annotated in both SMPL [24] and SMPL-X [33], AGORA has become an essential benchmark for evaluating 3D human mesh estimation models. It contains approximately 14K images with 107K instances for training, 1K images with 8K instances for validation, and 3K images for testing.

BEDLAM [3] is a large-scale, synthetic video dataset that includes a diversity of body shapes, motions, skin tones, hair, and clothing. The dataset contains approximately 286K images with 951K instances for training and 29K images with 96K instances for validation. For our ablation study, we uniformly downsample the training set by a factor of 6, resulting in 48K images with 159K instances. We do not use the test set because the SMPL format is not currently supported by the leaderboard.

COCO [20], **Crowdpose** [17], and **MPII** [1] are real-world multi-person datasets widely used for 2D human pose estimation tasks. We use these datasets for training to enhance the generalization capability of our model on real-world images by using pseudo annotations from NeuralAnnot [30] and only supervise projected 2D joints due to 3D ambiguity and their label noisiness. We uniformly downsample COCO by a factor of 4, resulting in 16K images with 66K instances for training. For Crowdpose, we use 10K images with 36K instances, and for MPII, we use 17K images with 29K instances.

H3.6M [13] is an indoor single-person dataset with 3D pose annotations. It contains videos of common activities performed by professional actors. We uniformly downsample its training set by a factor of 10 and use 31K images.

3DPW [48] is an in-the-wild dataset with 3D mesh annotations. It contains approximately 17K images for training and 24K images for testing. Following [2, 44, 45], we use the training set to finetune our model before evaluating the test set.

MuPoTS [28] is a real-world multi-person 3D pose dataset

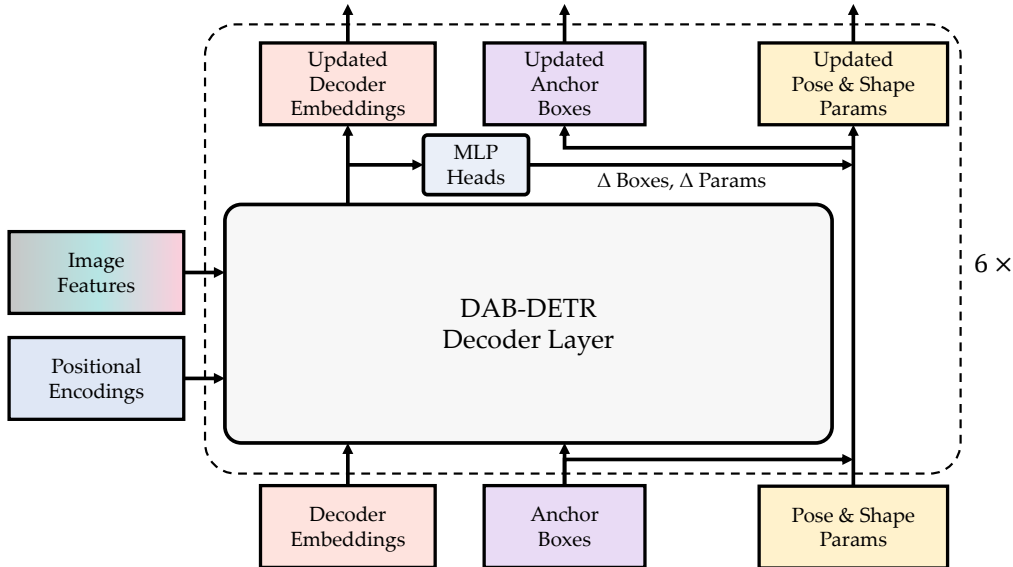


Figure A1. **Illustration of our decoder architecture.** Queries consist of *decoder embeddings* and *anchor boxes* following DAB-DETR [23]. Besides updating anchor boxes, we also update SMPL parameters using corresponding prediction heads.

composed of more than 8K frames from 20 scenes, each containing up to three subjects, annotated with 3D pose. Following previous works [2, 45], we only use it to evaluate the generalization capability of our model.

CMU Panoptic [15] is an indoor multi-person dataset providing 3D pose annotations. It contains 4 sequences of multiple people engaging in different social activities, with approximately 9K images. Following previous works [2, 44, 45], we only use it to evaluate the generalization capability of our model.

B. Extended Results

B.1. Ablation Study

Speed-accuracy trade-off. We evaluate the speed-accuracy trade-off across various ablation models. Specifically, we compare single-resolution baselines with our model, which adopts different processing strategies for background tokens (\mathcal{T}_B). In Tab. B1, we report the average number of tokens, inference runtime, and the MVE metric on the BEDLAM validation set [3]. The average number of tokens is included to highlight the impact of image tokens on inference speed.

In ablation (a), our baseline model with a resolution of 1288 achieves the lowest estimation error but suffers from redundant image tokens, leading to extremely slow inference. In contrast, ablation (b) shows faster inference but with poor performance, *i.e.* much higher MVE. In (d), simply replacing small-scale tokens with their high-resolution counterparts brings a noticeable boost in performance with additional overhead, where some low-resolution tokens are still redundant. In (f), our proposed method of pooling background

tokens \mathcal{T}_B once counteracts the overhead brought by high-resolution tokens, yielding similar performance. However, further reducing \mathcal{T}_B brings no significant acceleration and may result in a potential performance drop, as illustrated in (c) and (e). These results demonstrate that our scale-adaptive strategy achieves the best speed-accuracy trade-off, making our method the **best real-time model**.

Scale threshold α_s . To further study the impact of high-resolution tokens, we conduct experiments on various scale thresholds α_s while retaining the pooling of background tokens. $\alpha_s = 0$ denotes that no high-resolution tokens are used. Results are shown in Tab. B2. Compared to (a), (c) shows that our method achieves a consistent error reduction across different scale ranges, indicating that introducing sufficient high-resolution tokens eases the estimation challenge on small-scale instances and also allows the model to deal better with large-scale instances. In (b), although the improvement in the scale range of 0-30% is significant, the decrease in high-resolution samples increases learning difficulty during training and potentially leads to worse performance on larger-scale instances than (a). In (d), a large scale threshold ignores plenty of background context since the high-resolution tokens are encoded independently for N_{hr} layers, leading to a performance decline, which is consistent with our findings in Sec. 4.4.

B.2. Additional Qualitative Results

Scale-adaptive tokens. We present additional visualized examples of our scale-adaptive tokens \mathcal{T}_{SA} in Fig. B2. The last two cases include instances with scales near the scale threshold α_s , resulting in mixed-resolution token represen-

Table B1. **Speed-accuracy trade-off among different ablation settings.** We conduct our studies on BEDLAM [3] validation set, reporting the average number of different tokens, inference runtime and MVE.

| Ablation | Number of tokens | | | Runtime (ms) | MVE ↓ |
|-----------------------------------|------------------|----------------|------------|--------------|-------|
| | High-resolution | Low-resolution | Background | | |
| Single Resolution | | | | | |
| (a) Res. 1288 | 4784 | | | 174.9 | 53.2 |
| (b) Res. 644 | 1196 | | | 42.3 | 63.3 |
| Background Tokens \mathcal{T}_B | | | | | |
| (c) Drop all | 493 | 40 | 0 | 39.7 | 57.2 |
| (d) No pooling | 493 | | 1073 | 54.1 | 56.1 |
| (e) Pooling×2 | 493 | 94 | 100 | 41.6 | 56.3 |
| (f) Ours | 493 | 94 | 245 | 42.0 | 56.0 |

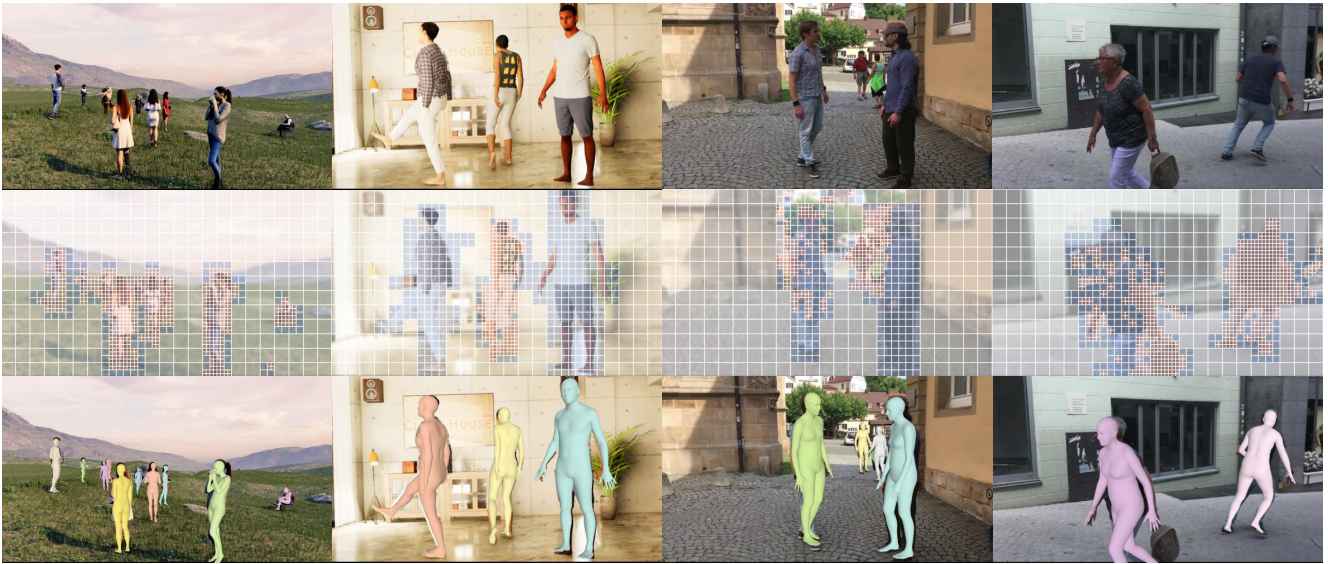


Figure B2. **Additional visualization of scale-adaptive tokens \mathcal{T}_{SA} .** We display the input, scale-adaptive tokens and the estimated mesh overlay (top to bottom). Tokens are visualized the same way as Fig. 6. The first two columns are qualitative results on synthetic datasets [3, 32], and the last two columns are on 3DPW [48].

Table B2. **Comparison of different scale thresholds on BEDLAM [3] validation set.** We report MVE for different scale ranges and the average (Avg.).

| α_s | 0-30% | 30-50% | 50-70% | 70%+ | Avg. |
|-----------------------|-------|--------|--------|------|------|
| (a) 0.0 | 67.0 | 60.4 | 58.6 | 64.0 | 64.0 |
| (b) 0.3 | 60.0 | 61.9 | 59.9 | 65.8 | 60.8 |
| (c) 0.5 (Ours) | 55.6 | 56.0 | 57.6 | 63.1 | 56.0 |
| (d) 0.7 | 55.9 | 56.1 | 58.2 | 65.2 | 56.2 |

tations for those individuals. Nevertheless, our model still produces satisfactory predictions, demonstrating the robustness and consistency of the features learned across different resolution levels.

SOTA comparisons. Fig. B3 and Fig. B4 present visual

comparisons between our method and existing SOTA approaches [2, 43–45] on synthetic images and real-world images, respectively. Our method demonstrates a strong generalization capability with accurate estimations across different scenarios. Specifically, our method can accurately estimate individuals across different scales, whereas other methods may fail to detect very small individuals or produce inaccurate estimations. See Fig. B4 for qualitative examples illustrating this advantage.

Failure cases. Fig. B5 (top) indicates that our method can result in unsatisfactory depth reasoning without explicit height or age awareness. Fig. B5 (bottom) shows poor mesh estimations on challenging scenes with heavy occlusion and complex human poses, which also challenges existing SOTA methods [2, 43].



Figure B3. **Comparison on synthetic images.** We compare our method with other SOTA methods [2, 43] on BEDLAM [3] (left) and AGORA [32] (right). Red dashed circles highlight areas with 2D misalignment or misdetection. The last row shows the elevated view of our estimations. Please zoom in for details.

B.3. Discussion

Multi-person 3D human mesh estimation is a fundamental task with broad applications. With recent one-stage SOTA methods [2, 43] achieving remarkable improvements in accuracy, we further explore the potential of DETR-style pipeline by leveraging scale-adaptive tokens to encode features more efficiently. Our approach achieves superior performance with significantly lower computational cost, marking a step forward for real-time applications. With more diverse training data of high quality GTs, we may further enhance our model’s robustness and generalization capability. Additionally, our scale-adaptive tokens may be able to be plugged into other DETR-style works to improve their efficiency in the future.

Limitations. Since our method is not age- or height-aware, it may produce larger depth estimation errors for children, as shown in Fig. B5 (top). In the future, this issue could be addressed by incorporating a mechanism to identify and account for children. Also, we currently only support body-

only estimation. Since regions of human face and hands are also challenging and require a higher resolution, our method can be extended to full-body estimation in the future.

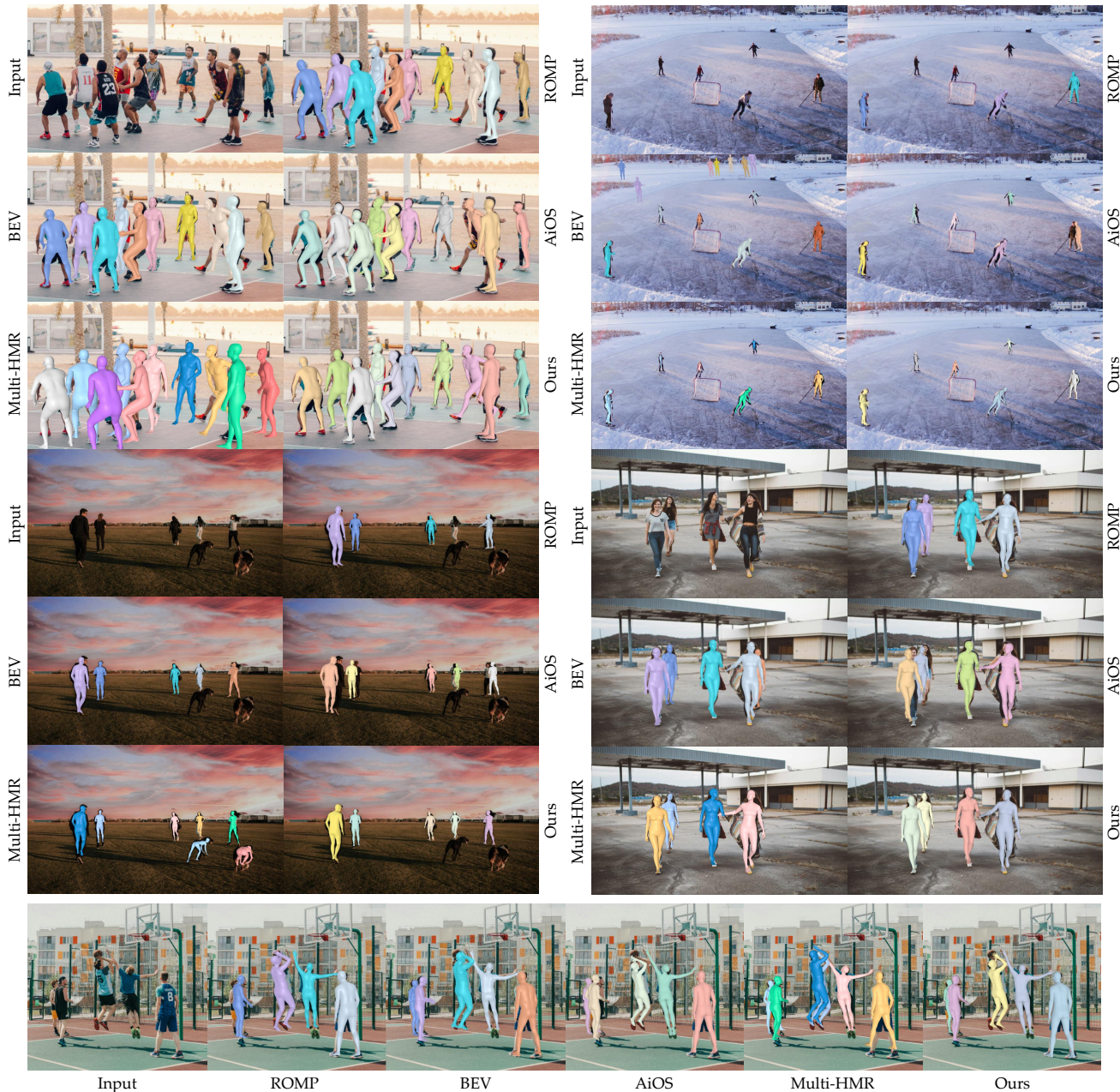


Figure B4. **Comparison on real-world images.** We compare our method with SOTA methods [2, 43–45] on in-the-wild images from the Internet. Our method outperforms all of them, especially in small-scale cases. Please zoom in for details.

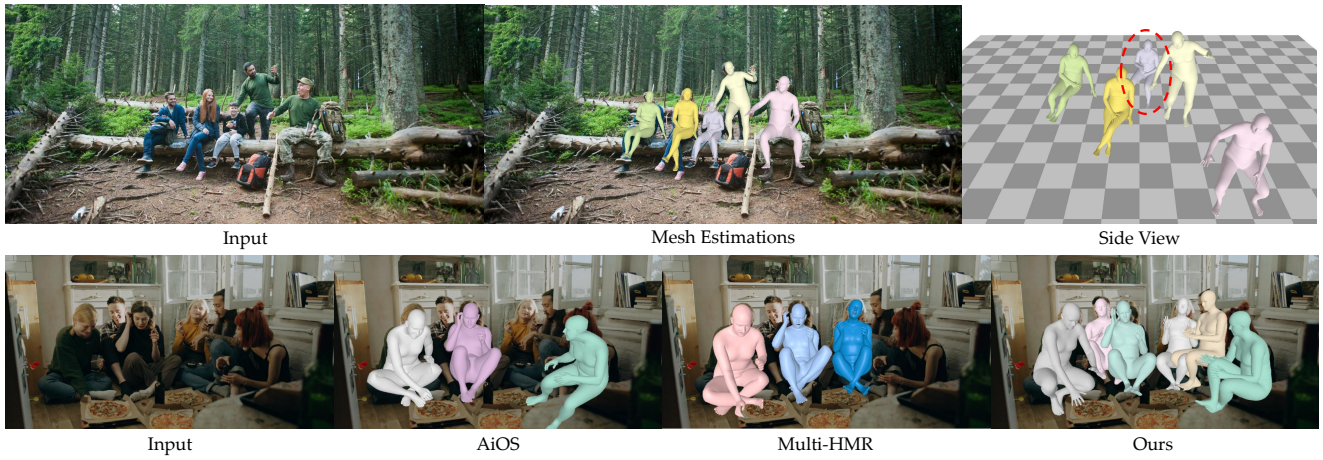


Figure B5. **Failure cases.** The top row shows an example of improper depth reasoning for the child. The bottom row shows poor estimation results of current SOTA methods in complex human poses and scenarios.